Solid Freeform Fabrication 2017: Proceedings of the 28th Annual International Solid Freeform Fabrication Symposium – An Additive Manufacturing Conference
Reviewed Paper

Modeling of crack propagation in 2D brittle finite lattice structures assisted by additive manufacturing

Yan Wu, Li Yang
Department of Industrial Engineering, University of Louisville, Louisville, KY 40292

Abstract

The failure characteristics of lattice structures are of significant importance in various lightweight applications such as aerospace and biomedicine. In this study, several 2D lattice structures with different number of unit cells that represent different geometrical characteristics and deformation mechanisms were investigated for their fracture behaviors. The fracture characteristic of the cellular samples was studied experimentally through tensile testing. The fracture propagation patterns of different lattice designs were investigated by high-speed camera, and consequently analyzed via analytical model in order to evaluate the effect of finite unit cells on the fracture characteristics of these cellular structures. The results were further compared with the classic cellular fracture theory by Gibson and Ashby. The comparison results suggest that for small number of unit cells designs the homogenized fracture model does not provide accurate crack propagation predictions.

1. Introduction

Cellular structures are networks of interconnected struts or walls with porosities, and they are widely found in many natural load-bearing structures. Besides light weighting, cellular structures also exhibit many attractive engineering properties including high performance-to-weight ratios, high energy absorption and damping, controlled thermal conductivities and high surface area-to-volume ratios, which make them highly promising in a wide range of applications including aerospace, biomedical and automobile structures or components.

In the design of periodic cellular structures, various geometries have been investigated for their mechanical properties including Poisson's ratio, Young's modulus, ultimate strength and yield strength [1-10]. The fracture properties of the cellular structures have been studied previously, although most of the efforts were focused on the fracture toughness of infinite cellular structures or cellular patterns with large number of unit cells. The research of Ashby [11] and Maiti [12] with the modeling of cellular fracture set the approach for most of the subsequent researches of this subject. Ashby [11] estimated the fracture toughness of a hexagonal lattice structure subjected to a remote stress, and it was assumed that the critical strut directly ahead of the macroscopic crack tip would fail when its stress level reaches the ultimate material strength following the approach employed by the conventional linear elastic fracture mechanics. M.R. O'Masta [13] investigated the fracture toughness of a Ti-6Al-4V alloy octet-truss lattice structure manufactured using a 'snap-fit' method in which layers of out of plane pyramidal trusses were combined with open face sheets of planar octet-truss and the process repeated to create samples of arbitrary dimensions. Hamza Alsalla [14] studied the effect of different build directions of the 316L lattice structure on the fracture toughness properties,

which were compared to the Ashby and Gibson models. P. Maimí [15] analyzed the crack propagation in quasi-brittle two-dimensional isotropic lattices and found that there existed a critical truss length above which the crack propagation mechanism changes from energy dissipation driven to stress field driven. In most studies, the cellular structures can be treated as a continuous medium with equivalent mechanical properties so that the linear elastic fracture mechanics can be applied for analysis. However, such treatment does not always represent the real applications where cellular structures with relatively small sizes are designed. When taking the size effect into consideration, especially for those who have small number of unit cells, the continuum assumption will no longer hold, and the linear elastic fracture mechanics becomes inapplicable. In the modeling of cellular structures, the infinite structure assumption also implies maximum symmetry conditions of the structures, which facilitates the simplification of the structures for analytical modeling [5]. However, in the case of the finite structures, due to the need to account for boundary effects, such simplification could not be applied, which poses challenge for the effective modeling of the cellular structures.

Both stress intensity factor [11, 16] and energy release rate [15, 17] have been used for the modeling of cellular structure fracture toughness by treating the infinite cellular structure as the continuum solids. The stress intensity factor is based on the stress state near the tip of a crack caused by a remote load or residual stresses, and the energy release rate is based on the energy dissipation during fracture per unit of newly created fracture surface area. When analyzing the fracture properties of the cellular structures under remote stresses, the model of Ashby and Gibson [12, 18, 19] utilizes the stress intensity factor for the modeling of fracture toughness. Besides, P. Maimí [15] found that stress intensity factor and energy release rate worked at different intervals of the strut length of the cellular structure when analyzing the crack propagation. But their work was still focusing on the infinite structures. Therefore, another challenge for the analytical modeling of finite unit cell structure fracture to identify the appropriate failure criterion for the crack propagation.

In the present paper, attempts were made to model fracture pattern of the 2D lattice structures by taking the size effect into consideration. The matrix displacement method was used for the analytical calculations. For the failure criterion in the analytical model, the method based on stress criteria and the method based on strain energy criteria will be both evaluated. Some 2D lattice structures (rhombus and honeycomb shown in Fig. 1) with different unit cell numbers that represent different geometrical characteristics and deformation mechanisms were investigated for their fracture behaviors. The fracture characteristic of the cellular samples was studied experimentally through tensile testing. The fracture propagation patterns of different lattice designs were investigated by high-speed camera, and consequently analyzed via analytical model in order to evaluate the fracture characteristics of these finite-sized cellular structures. The results were further compared with the classic cellular fracture theory, which were used to evaluate the effectiveness of the classic fracture model for the small-size cellular designs.

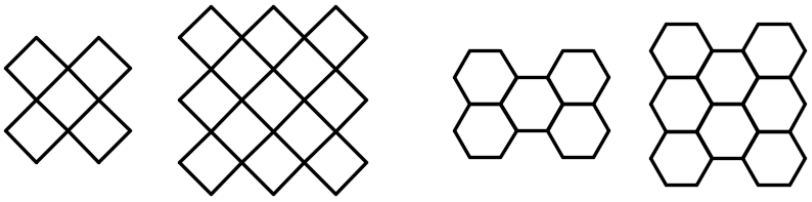

(a) (b) (c) (d)

Fig. 1 (a) 2X2 Rhombus; (b) 3X3 Rhombus; (c) 2X3 Honeycomb; (d) 3X3 Honeycomb

2. Fracture properties modeling

2.1 Matrix displacement method

Firstly, the matrix displacement method will be used for the analytical model. Each slender strut is considered to be rigidly connected at the nodes. For each node, there are three degrees of freedom/ displacements, which are axial displacement, vertical displacement and the rotational angle. The respective forces are the axial force, shear force and the moment. Each strut is consisted of two nodes, which means there are six displacements as shown in Fig.2.

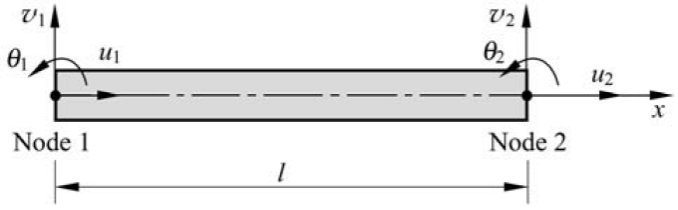

Fig. 2 The strut element with two nodes under local coordinate system

For a single strut element, there exists a relationship between the nodal displacement vector $[d]^e$ in Eq. (1) and the nodal force vector$[F]^e$ Eq. (2), shown in Eq. (3).

$$[d]^e = [\ u_1\ v_1\ \theta_1\ u_2\ v_2\ \theta_2\ ]^T \tag{1}$$

$$[F]^e = [\ F_{x1}\ F_{y1}\ M_1\ F_{x2}\ F_{y2}\ M_2\ ]^T \tag{2}$$

$$[\mathrm{K}]^e \cdot [\mathrm{d}]^e = [\mathrm{F}]^e \tag{3}$$

Combining the bar stiffness matrix and pure bending beam stiffness matrix, the element stiffness matrix $[\mathrm{K}]^e$ for a six degrees of freedom strut is shown in Eq. (4),

$$\mathbf{K}^{e}_{(6\times6)} = \begin{bmatrix} \frac{EA}{l} & 0 & 0 & -\frac{EA}{l} & 0 & 0 \\ 0 & \frac{12EI}{l^3} & \frac{6EI}{l^2} & 0 & -\frac{12EI}{l^3} & \frac{6EI}{l^2} \\ 0 & \frac{6EI}{l^2} & \frac{4EI}{l} & 0 & -\frac{6EI}{l^2} & \frac{2EI}{l} \\ -\frac{EA}{l} & 0 & 0 & \frac{EA}{l} & 0 & 0 \\ 0 & -\frac{12EI}{l^3} & -\frac{6EI}{l^2} & 0 & \frac{12EI}{l^3} & -\frac{6EI}{l^2} \\ 0 & \frac{6EI}{l^2} & \frac{2EI}{l} & 0 & -\frac{6EI}{l^2} & \frac{4EI}{l} \end{bmatrix} \tag{4}$$

where E, A, l and I are Young's modulus, area of the cross section, length of the strut and the second moment of inertia. $[\mathrm{K}]^e$ is a factor that is only decided by the structure and material and has no dependency on the applied forces.

Since $[\mathrm{K}]^e$ is based on the local coordinate system as shown in Fig.2, and for cellular structures individual struts are likely orientated differently, additional transformation is needed to convert the stiffness matrix into more consistent global coordinate system. Therefore, the transformation matrix $[T]^e$ shown in Eq. (5) was introduced to convert the different local coordinate system to a global coordinate system.

$$\mathbf{T}^{e}_{(6\times6)} = \begin{bmatrix} \cos\alpha & \sin\alpha & 0 & 0 & 0 & 0 \\ -\sin\alpha & \cos\alpha & 0 & 0 & 0 & 0 \\ 0 & 0 & 1 & 0 & 0 & 0 \\ 0 & 0 & 0 & \cos\alpha & \sin\alpha & 0 \\ 0 & 0 & 0 & -\sin\alpha & \cos\alpha & 0 \\ 0 & 0 & 0 & 0 & 0 & 1 \end{bmatrix} \tag{5}$$

Apply such transformation to the applied forces and the displacements, and the results is shown in Eq. (6) and (7).

$$[d]^e = [T]^e \cdot [\bar{\mathrm{d}}] \tag{6}$$

$$[F]^e = [T]^e \cdot [\bar{\mathrm{F}}] \tag{7}$$

Where $[d]^e$ and $[F]^e$ are under local coordinate system and $[\bar{d}]$ and $[\bar{\mathrm{F}}]$ are under global coordinate system. Substituting Eq. (6) and (7) into Eq. (3) and equating the expression for $[\mathrm{K}]$ which is the stiffness matrix under global coordinate system, we have

$$[\bar{\mathrm{K}}] = [T]^{eT} \cdot [\mathrm{K}]^e \cdot [T]^e. \tag{8}$$

Then one can simply add all the $[\overline{\mathrm{K}}]$ together to get the whole stiffness matrix $[\overline{\mathrm{K}}]$ as shown in Eq. (9).

$$[\mathrm{K}] = \sum_{i=1}^{n} [\overline{K}]_i \tag{9}$$

where n is the total number of all the trusses of the structure.

It is noted that the 2D lattice structures are usually subjected to the loading conditions that are applied on the boundaries, and there does not exist external forces at the internal nodes as shown in Fig. 1. This means that on the boundaries most of the displacements are either zero or known values, and the external forces are always zero at the internal nodes. Therefore, for 2D lattice structures the displacements $[\mathrm{d}]$ and forces $[\mathrm{F}]$ can be divided into the known part and unknown part for further calculation. Therefore, the stiffness matrix Eq. can be rewritten as

$$\begin{bmatrix} A_{11} & A_{12} \\ A_{21} & A_{22} \end{bmatrix} \begin{bmatrix} d_1 \\ d_2 \end{bmatrix} = \begin{bmatrix} F_1 \\ F_2 \end{bmatrix} \tag{10}$$

where d_1 is the vector of unknown displacements, d_2 is the vector of known displacements, F_1 is a vector of known forces and F_2 is a vector of unknown forces. From Eq. (10), the unknown displacements can be solved as

$$d_1 = {A_{11}}^{-1}(F_1 - A_{12}d_2). \tag{11}$$

Therefore, with the knowledge of d_2, all the displacement components can be determined for the calculation of the internal forces for each strut.

2.2 Stress-dominated propagation model

From the force equilibrium conditions in Fig. 3(a), the shear force is constant along the beam with the same direction as shown in Fig. 3(b). The moment is shown in Fig. 3(c), which achieves the maximum value at two nodes.

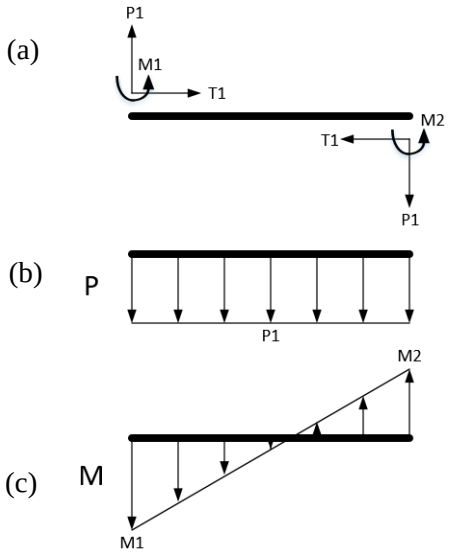

Fig. 3 (a)The force equilibrium of the beam; (b)The shear force distributed along the beam; (c) the moment distributed along the beam

Since each strut is subject to the combination of in-plane normal stresses and shear stress, the principal stresses analysis will be used to model the plastic failure of the struts. The normal stresses consists of two components, which are contributed by the normal stresses and the axial force as shown in Fig. 4(a) and (b).

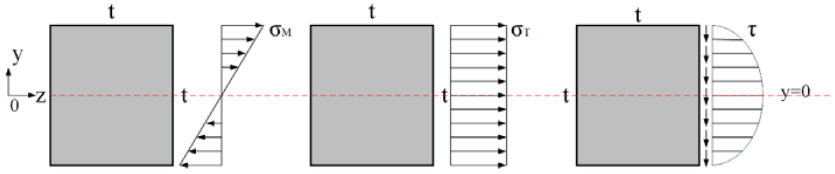

(a) (b) (c)

Fig. 4 (a) The normal stress caused by moment; (b) The normal stress caused by axial force; (c) The shear stress caused by shear force

For the normal stress contributed by the moment, the distribution of the normal stress can be expressed as

$$\sigma_M = \frac{M * y}{I_z} \ , \tag{12}$$

where the M is the moment at each cross section, and y is the distance of the point from the neutral plane. It is obvious that the maximum σ_M is achived at the upper/lower surfaceson the plane that has the maximum moment, which can be readily determined from strut force analysis (Fig. 3(c)).

In addition, the normal stress contributed by the axial force can be calculated as

(13)

$$\sigma_T = \frac{T}{A} \ ,$$

where T is the axial force of the truss and A is the area of the cross section.

The shear stress contributed by the shear force, is a function of the shear force (P) and the distance of the point of interest from the neutral plane(y), which can be obtained from

$$\tau = \frac{P}{2I_Z}\left(\frac{t^2}{4} - y^2\right), \tag{14}$$

where t is the width of the cross section and

$$I_Z = \frac{t^4}{12} \ . \tag{15}$$

Therefore, the total normal stress σ is determined by Eq.(16), and the total shear stress is determined by Eq.(14).

$$\sigma = \sigma_T + \sigma_M = \frac{M * y}{I_z} + \frac{T}{A}. \tag{16}$$

The principal stress σ_1 can be written in terms of σ_T and σ_M shown in Eq. (17), which achieves maximum value at the distance $y = t/2$. When the maximum principal stress reaches the yield strength, the structure starts to yield. For brittle material, it can be considered that $\sigma_Y=\sigma_U$, where σ_U is the ultimate strength of the material. Therefore, by equating σ_1 to σ_Y, the maximum stress conditions of the struts can be determined by Eq.(17).

$$\sigma_1 = \frac{\sigma}{2} + \sqrt{\frac{\sigma^2}{4} + \tau^2} = \frac{1}{2}\left(\frac{M * y}{I_z} + \frac{T}{A}\right) + \sqrt{\frac{1}{4}\left(\frac{M * y}{I_z} + \frac{T}{A}\right)^2 + \frac{P^2}{4{I_Z}^2}\left(\frac{t^2}{4} - y^2\right)^2}. \tag{17}$$

By calculating the principle stresses of every struts in the cellular structure, the maximum stress point of the whole structure can be identified, which will be considered as the strut to fail. After the strut fails, the stress would redistribute, and the stress status of individual struts must be re-calculated. By using the displacement matrix method above, the next strut to fail was then calculated by the same manner. Through this iterative process, the sequence of the trusses to crack were calculated until the entire structure failed.

2.3 Energy-dominated propagation model

For the continuum solids, the energy release rate indicates the energy dissipated per unit of newly created fracture surface area. The energy release rate failure criterion states that a

crack will grow when the available energy release rate G is greater than or equal to a critical value G_c. The quantity G_c is the fracture energy and is considered to be a material property which is independent of the applied loads and the geometry of the body. However, for the finite lattice structure, the structure is not continuous, and therefore the dissipated energy during the fracture is not a smooth function, which means that the Griffith's energy release rate cannot be used as the criterion for the crack propagation for the brittle lattice. Since the cross section is the same in all the trusses which means that the energy to generate a new surface is constant, the amount of energy release during the strut fracture was employed to evaluate the direction of the crack propagation. The strut for crack propagation would follow the criteria of maximum energy release.

For the traditional modeling of fracture for the continuum solid, a pre-existing crack will be assumed. Unlike the continuum solid, for the lattice structures the crack front is not well defined. In addition, the fracture propagation exhibits a discrete "stepwise" fracture mode due to the fracture of individual struts. Fig. 5 shows the stages during the fracture by taking the 2X2 rhombus structure as an example. Fig. 5(a) shows the original status of the structure before the stress is applied. From Fig. 5(a) to Fig. 5(b), the structure will store certain amount of strain energy $V_{\varepsilon 1}$. When the first strut cracks, the stress will redistribute, which results in strain energy $V_{\varepsilon 2}$ as illustrated in Fig. 5(c). Therefore, the energy release amount was taken as the difference between these two strain energies.

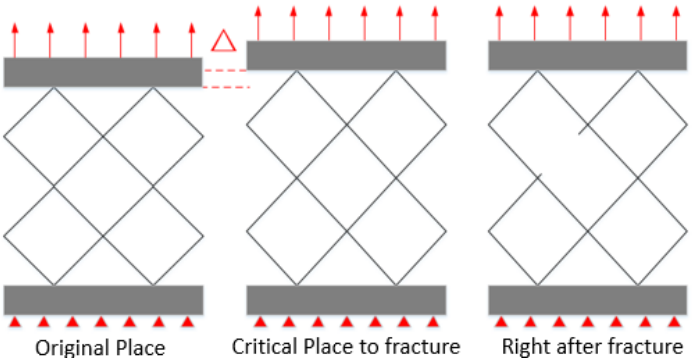

(a) (b) (c)

Fig. 5 Stages during fracture

Since the internal forces and moments are known from the displacement matrix method, the respective strain energy can be obtained from the Eq. (18).

$$V_{\varepsilon} = \int_0^l \frac{T^2(x)}{2EA} dx + \int_0^l \frac{M^2(x)}{2EI} dx \tag{18}$$

From Eq. (18), the crack propagation will be calculated using the maximum energy release criteria.

3. Predictions from the analytical model

The 2D rhombus structure and honeycomb as shown in Fig. 1 were used to evaluate the two different crack propagation mechanics. The thickness of each strut was designed to be parameter constant of 1mm. The angle between each strut in rhombus structure is 90 degrees and the angle between each strut in honeycomb structure is 120 degrees. The length of each strut was set to be 10mm to ensure the slenderness of the struts. By using the analytical model established above, the crack propagation paths of these structures were calculated.

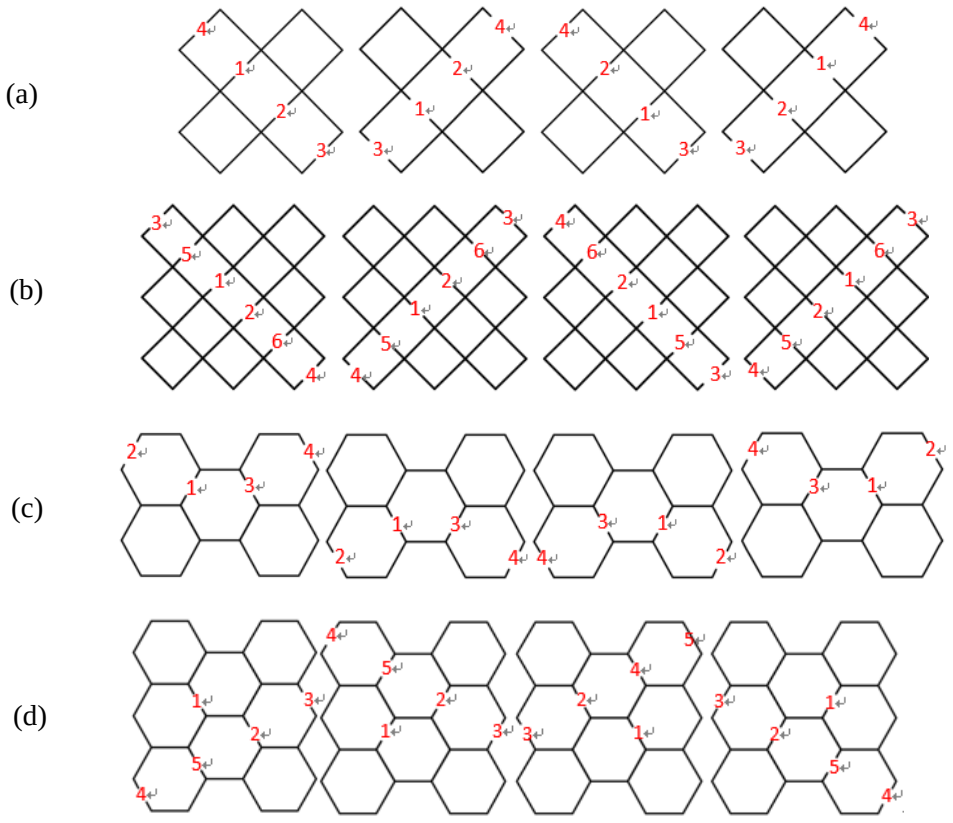

Fig.6 Four crack propagation modes

Fig. 6 shows four crack propagation modes based on the analytical model. Both of the stress-dominated model and the energy-dominated model give the same predictions for the two lattice structures. For the rhombus structure, due to the structural symmetry, the maximum stress and the maximum energy release were both achieved by the fracture of either of the four struts in the center unit. Fig. 6(a) and Fig. 6(b) illustrate the fracture propagation paths for the rhombus structures staring from each of these four struts. For the 2X2 rhombus structures shown in Fig. 6(a), the fracture pattern exhibits very predictable pattern that runs diagonally. The 3X3 rhombus structure shown in Fig. 6(b) exhibits the similar fracture pattern as the 2X2 rhombus structure. However, the 3X3 rhombus have more struts than the 2X2 rhombus structure, which leads to more crack propagation patterns even though the final crack pattern remains the same. For example, after strut 1 and 2 in Fig. 6(b) fractured, the strut 3 and 4 had the same stress level due to the symmetry, which means that either of these two struts would be the next one to

fracture. The same argument also applies to strut 5 and 6, and they had the same probabilities to be the next one to fracture. Accounting for all the probabilities would result in more crack propagation patterns. For the two honeycomb structures in Fig. 6(c) and (d), although the fracture pattern was different from the rhombus structures, the fracture also exhibits regular pattern that varies as the number of unit cells changes.

Although in the previous cases both fracture models yield the same fracture pattern predictions, they exhibit different sensitivity to the property variabilities in the struts. In order to estimate such difference, the most critical struts and second most critical struts using both the maximum stress and energy release methods during each of the first two steps of the crack propagation were evaluated. When the second maximum stress or energy release amount become very close to the first maximum values, the second critical struts would be more likely to fracture if there exist some fabrication defects with the most critical struts. The sensitivity of such phenomenon can be estimated by a sensitivity index, which is the difference between the first and second maximum values divides by the first maximum value, which is shown in Table 1. Higher sensitivity index indicates that the fracture is less sensitive to the manufacturing defects. From Table 1, it is obvious that the sensitivity became smaller when the number of fractured trusses grew for both stress method and energy method, which indicates that as the crack propagation advances the uncertainty of fracture pattern caused by the manufacturing quality reduces. Besides, the sensitivity became higher when structure size increases from 2X2 to 3X3 for rhombus and 2X3 to 3X3 for honeycomb, which indicates that for larger cellular structures the fracture is more sensitive to manufacturing quality. Furthermore, when comparing the differences between stress method and energy method, the sensitivity based on energy method was significantly higher than that based on stress method. This can be conceptually explained from the definition of these two method. For stress-dominated method, the maximum stress level alone determines the fracture criticality. However for energy-dominated method, the strain energy is calculated for the entire structure. Therefore, from this perspective the energy-dominated method focuses on the evaluation of the averaged qualities of the structure, while the stress-dominated stress focuses on the maximum stress concentration effect on individual struts.

Structures	Fractured Strut	Sensitivity index (%)	
		Stress Method	Energy Method
2X2 Rhombus	1	9.36	2.31
	1+2	14.28	5.36
3X3 Rhombus	1	6.57	1.95
	1+2	10.26	4.56
2X3 Honeycomb	1	5.56	1.84
	1+2	7.12	2.68
3X3 Honeycomb	1	4.12	1.26
	1+2	5.89	2.10

Table 1. The sensitivity index of the first and second maximum stress and energy release methods for different structures

4. Experiment results

In the experimental verification of the fracture characteristics, in order to reduce the anisotropic effect and quality variability of the cellular samples, all the samples were fabricated via stereolithography using the Formlabs 2 printer using the black resin. Three samples were fabricated for each structure. The parts were shown in Fig. 8. To ensure that the parts exhibit brittle fracture, all samples were put in the oven with the temperature of 130 degree for 4 hours. The Young's modulus of this black resin is 2.8GPa after the over-curing process.

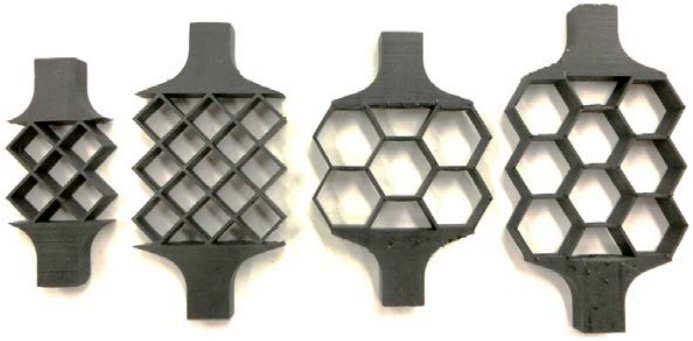

Fig.8 Samples printed by Formlabs Form 2

The tensile testes were carried out on an Instron 5569A tensile tester with the crosshead speed of 0.3 mm/min. The fracture propagation patterns were captured via a digital camera and analyzed afterwards. Fig. 9 shows the results for the crack propagation. The results show that the crack propagation for most of the sample agrees with the predictions from Fig. 6.

(a)

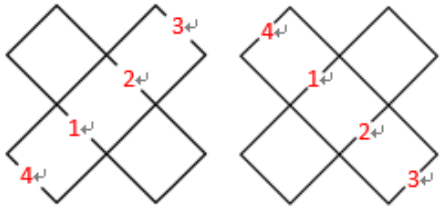

(b)

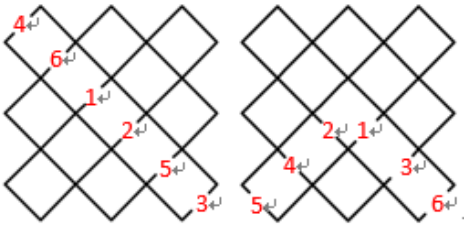

(c)

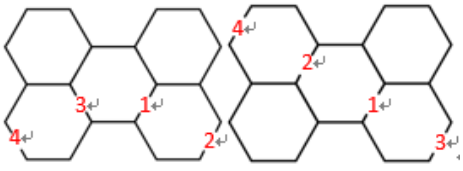

(d)

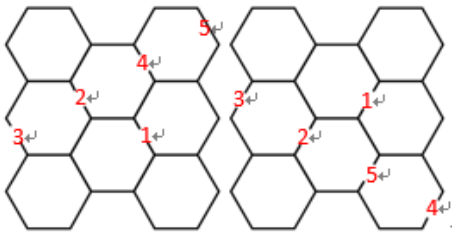

Fig. 9 Experimental results for the crack propagations

Fig. 9(a) shows the crack propagations for the 2X2 rhombus structures. Two samples exhibit the pattern shown in the first picture and one sample exhibit the pattern shown in the second picture. The experimental crack propagation pattern were consistent with the predictions shown in Fig. 6(a). Fig. 9(b) shows the crack propagations for the 3X3 rhombus structures. Two samples exhibit the pattern shown in the first picture, which agrees with the predictions shown in Fig. 6(b). However, the second picture showed another pattern exhibited by the third sample, which did not agree with the predictions. From the previous analysis of the fracture pattern sensitivity, the critical strut which was expected to fracture according to the analytical model had a very similar stress and energy release amount compared to the second critical strut that actual fractured. The differences were 9.36% and 2.31% respectively based on stress-dominated model and energy-dominated model. Furthermore, it was found that there existed some defect inside of the actual fractured strut shown in Fig. 10(a). Due to the deviation of the first crack propagation site, the rest of the crack propagation formed a new pattern due to the different stress distribution with the rest of the structure.

(a) (b)

Fig. 10 (a) Fractured truss section with defect; (b) Fractured truss section without defect

Fig. 9(c) shows the crack propagations for the 2X3 honeycomb structures. Two of the samples exhibit the pattern shown in the first picture that agrees with the analytical predictions. One of the samples had the same situation with the 3X3 rhombus structures. The fabrication defect rendered the fracture pattern to be slightly different from the analytical prediction. Fig. 9(d) shows the crack propagations for the 3X3 honeycomb structures. All the samples exhibit fracture patterns that are consistent to the analytical predictions in Fig. 6(d).

The experimental results showed that both the stress-dominated model and the energy-dominated model can provide correct predictions for the designed finite rhombus and honeycomb structures. Besides, for those samples which did not follow the analytical predictions, the sensitivity analysis can also provide additional insights into the cause of the altered fracture pattern.

Both the stress-dominated model and the energy-dominated model predicted the crack propagation patterns that were highly dependent on the evolving strut stress distribution. In comparison, using the model from Ashby and Gibson as shown in Fig.11 [18, 19], the predicted fracture pattern does not agree with the experimental results. For the two models proposed in this paper, the fracture of each unit cells was analyzed individually so that a more accurate crack propagation pattern could be obtained.

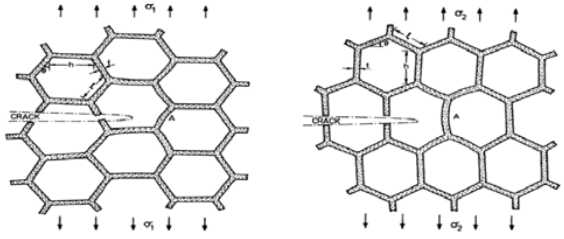

(a) (b)

Fig. 11 Fracture of infinite honeycomb structures: (a) fracture along 1st direction; (b) fracture along 2nd direction

5. Conclusions

In this paper the stress-dominated method and energy-dominated method were proposed to establish the crack propagation model of brittle 2D lattice with finite unit cells. For the 2X2 and 3X3 rhombus structure and 2X3 and 3X3 honeycomb structure, both modeling method predicted the same fracture patterns, although they exhibit different sensitivity to the manufacturing defects. The experimental results from tensile testing with the samples built using stereolithography process showed both method were efficient for the prediction of the crack propagation for finite unit cells structures.

Acknowledgement

The authors are grateful of the support from Rapid Prototyping Center (RPC) at University of Louisville. This project was partially supported by the Office of Naval Research (ONR) grant #N00014-16-1-2394.

Reference

[1] Yan, C., Hao, L., Hussein, A., Young, P., & Raymont, D. (2014). Advanced lightweight 316L stainless steel cellular lattice structures fabricated via selective laser melting. Materials & Design, 55, 533-541.

[2] Smith, M., Guan, Z., & Cantwell, W. J. (2013). Finite element modelling of the compressive response of lattice structures manufactured using the selective laser melting technique. International Journal of Mechanical Sciences, 67, 28-41.

[3] Li, S. J., Murr, L. E., Cheng, X. Y., Zhang, Z. B., Hao, Y. L., Yang, R., ... & Wicker, R. B. (2012). Compression fatigue behavior of Ti–6Al–4V mesh arrays fabricated by electron beam melting. Acta Materialia, 60(3), 793-802.

[4] Deshpande, V. S., Fleck, N. A., & Ashby, M. F. (2001). Effective properties of the octet-truss lattice material. Journal of the Mechanics and Physics of Solids, 49(8), 1747-1769.

[5] Yang, L., Harrysson, O., West, H., & Cormier, D. (2013). Modeling of uniaxial compression in a 3D periodic re-entrant lattice structure. Journal of Materials Science, 48(4), 1413-1422.

[6] Novak, N., Vesenjak, M., & Ren, Z. (2016). Auxetic Cellular Materials-a Review. Strojniški vestnik-Journal of Mechanical Engineering, 62(9), 485-493.

[7] Maskery, I., Aboulkhair, N. T., Aremu, A. O., Tuck, C. J., Ashcroft, I. A., Wildman, R. D., & Hague, R. J. (2016). A mechanical property evaluation of graded density Al-Si10-Mg lattice structures manufactured by selective laser melting. Materials Science and Engineering: A, 670, 264-274.

[8] Yang, L., Harrysson, O., West, H., & Cormier, D. (2015). Mechanical properties of 3D re-entrant honeycomb auxetic structures realized via additive manufacturing. International Journal of Solids and Structures, 69, 475-490.

[9] Yan, C., Hao, L., Hussein, A., Bubb, S. L., Young, P., & Raymont, D. (2014). Evaluation of light-weight AlSi10Mg periodic cellular lattice structures fabricated via direct metal laser sintering. Journal of Materials Processing Technology, 214(4), 856-864.

[10] Cheng, X. Y., Li, S. J., Murr, L. E., Zhang, Z. B., Hao, Y. L., Yang, R., ... & Wicker, R. B. (2012). Compression deformation behavior of Ti–6Al–4V alloy with cellular structures fabricated by electron beam melting. journal of the mechanical behavior of biomedical materials, 16, 153-162.

[11] Ashby MF (1983) The mechanical properties of cellular solids. Metall. Trans. 14(9): 1755-1769.

[12] Maiti SK, Ashby MF, Gibson LJ (1984) Fracture toughness of brittle cellular solids. Scripta Metallurgica 18(3): 213-217.

[13] O'Masta, M. R., et al. "The fracture toughness of octet-truss lattices." Journal of the Mechanics and Physics of Solids 98 (2017): 271-289.

[14] Alsalla, H., Hao, L., & Smith, C. (2016). Fracture toughness and tensile strength of 316L stainless steel cellular lattice structures manufactured using the selective laser melting technique. Materials Science and Engineering: A, 669, 1-6.

[15] Maimí, P., Turon, A., & Trias, D. (2011). Crack propagation in quasi-brittle two-dimensional isotropic lattices. Engineering Fracture Mechanics, 78(1), 60-70.

[16] Anderson, T.L. (2005). Fracture mechanics: fundamentals and applications. CRC Press.

[17] Griffith, A.A., "The Phenomena of Rupture and Flow in Solids," Philosophical Transactions, Series A, Vol. 221, pp. 163-198, 1920.

[18] Huang, J. S., & Gibson, L. J. (1991). Fracture toughness of brittle honeycombs. Acta metallurgica et materialia, 39(7), 1617-1626.

[19] Huang, J. S., & Gibson, L. J. (1991). Fracture toughness of brittle foams. Acta metallurgica et materialia, 39(7), 1627-1636.